RSC Advances

PAPER

View Article Online
View Journal | View Issue

Cite this: *RSC Adv.*, 2018, **8**, 31853

$NiO/Ni_xCo_{3-x}O_4$ porous ultrathin nanosheet/nanowire composite structures as high-performance supercapacitor electrodes†

Dongkai Jiang,[a] Maojun Zheng,*[ab] Yuxiu You,[a] Liguo Ma,[a] Pengjie Liu,[a] Fanggang Li,[a] Hao Yuan,[a] Zhihao Zhai,[a] Li Ma[c] and Wenzhong Shen[a]

Received 6th June 2018
Accepted 21st August 2018

DOI: 10.1039/c8ra04827d

rsc.li/rsc-advances

The demand for a new generation of high-safety, long-lifespan, and high-capacity power sources increases rapidly with the growth of energy consumption in the world. Here we report a facile method for preparing architecture materials made of $NiO/Ni_xCo_{3-x}O_4$ porous nanosheets coupled with $NiO/Ni_xCo_{3-x}O_4$ porous nanowires grown *in situ* on nickel foams using a hydrothermal method without any binder followed by a heat treatment process. The nanosheet-shaped $NiO/Ni_xCo_{3-x}O_4$ species in the nanosheet matrix function well as a scaffold and support for the dispersion of the $Ni_xCo_{3-x}O_4$ nanowires, resulting in a relatively loose and open structure within the electrode matrix. Among all composite electrodes prepared, the one annealed in air at 300 °C displays the best electrochemical behavior, achieving a specific capacitance of 270 mF cm^{-2} at 5 mA cm^{-2} while maintaining excellent stability (retaining ≈ 89% of the max capacitance after 20 000 cycles), demonstrating its potential for practical application in power storage devices.

Introduction

Supercapacitors as promising energy storage devices have attracted a lot of attention in recent years because they have higher power density and cycle performance than lithium ion batteries.[1–4] They are being integrated into microelectronics, textiles and electric vehicles, transforming our lifestyle. Large-scale energy storage is helping to improve the intermittency problems with renewable energy sources such as solar, wind and wave.

Capacitive positive electrode materials made of nanosheet-shaped transition-metal compounds, such as metal oxides/hydroxides and layered double hydroxides (LDH), without additives, have been demonstrated to hold great potential for advanced supercapacitors.[5] This kind of electrode without any binders or conductive agents can effectively cut down the "dead surface" in conventional slurry-derived electrodes, facilitate more efficient charge and mass transportation, and simplify the electrode-preparation process.[6] Moreover, compared to traditional bulky materials, the 2D nanosheet-shaped transition metal compounds aid in shortening the transport distance of the ions because of their large aspect ratio and can further improve the utilization of the active materials.

Among these metal oxides and hydroxides materials, NiO[7,8] and $Ni(OH)_2$ (ref. 9) have attracted a lot of attention due to their high theoretical capacitance, excellent chemical stability, low cost and low toxicity.[10] However, the comparatively poor electrical conductivity of NiO (0.01–0.32 S m^{-1})[11] or $Ni(OH)_2$ is the major defect as the electrode material. Thus, cobalt ions can be introduced into NiO or $Ni(OH)_2$, which can improve the conductivity of electrode materials because Co^{2+} can be oxidized to conductive CoOOH (12.8 S cm^{-1}) during the redox reaction process.[12] The addition of cobalt ions is also helpful to raise the oxygen overpotential helpful with widening potential window.[13] What's more, the slow kinetics of faradaic reactions of NiCo-based materials is another factor that limits their electrochemical performance.[14] It is desirable to develop NiCo-based electrodes with large ion accessible surface area. Previous studies have primarily been focused on development of NiCo-based nanomaterials with controlled morphology and enhanced surface area, such as nanosheets,[15,16] nanowires,[17] nanoflowers[18] and nanorods.[1,15] However, the simple and convenient methods to prepare large scale composite porous nanostructures are rarely reported, while it is valuable for practical applications.

In this paper, we report a simple process for large-scale fabrication of self-standing composite film electrodes composed of cobalt doped nickel oxide $NiO/Ni_xCo_{3-x}O_4$ porous ultrathin nanosheet/porous nanowire composite structure for

[a]Key Laboratory of Artificial Structure and Quantum Control, Ministry of Education, School of Physics and Astronomy, Shanghai Jiao Tong University, Shanghai, 200240, PR China. E-mail: mjzheng@sjtu.edu.cn; Fax: +86-021-54741040

[b]Collaborative Innovation Center of Advanced Microstructures, Nanjing University, Nanjing, 210093, PR China

[c]School of Chemistry and Chemical Technology, Shanghai Jiao Tong University, Shanghai, 200240, PR China

† Electronic supplementary information (ESI) available. See DOI: 10.1039/c8ra04827d

supercapacitors. The flexible Ni-foam plays a dual role both as the current collector and the substrate of the architecture materials. Owing to this unique nanosheet/nanowire composite structure, the one annealed in air at 300 °C displays the best electrochemical behavior, which can achieve a specific capacitance of 270 mF cm^{-2} at 5 mA cm^{-2} after 10 000 cycles and maintain the excellent cycling stability of the electrode that remains about 89% of the max capacitance after 20 000 cycles at the current density of 5 mA cm^{-2}.

Experimental section

Synthesis of the NiO/$Ni_xCo_{3-x}O_4$ porous nanowires/porous nanosheet composite structure on nickel foam

A piece of nickel foam, 1 cm × 1.5 cm, was respectively cleaned by acetone, absolute ethanol and deionized water in an ultrasound bath. For a typical run, $Ni(NO_3)_2 \cdot 6H_2O$ (4.2 mmol), $Co(NO3)_2 \cdot 6H_2O$ (1.4 mmol) (Ni/Co molar ratio 3 : 1), and HMT (5.6 mmol) were dissolved into distilled water (100 mL) at room temperature, and the solution was then transferred into a Teflon-lined stainless steel autoclave (200 mL). The Ni-foam substrate was then immersed into the solution and kept in an electric oven at 120 °C for 24 h. The autoclave was then removed from the oven and cooled to room temperature. The precursor was washed thoroughly with water and ethanol, and finally dried at 80 °C in air for 12 h, yielding the precursor nanohybrids on the Ni-foam. Subsequently, the NiO/$Ni_xCo_{3-x}O_4$ porous nanosheet/nanowire composite structure were obtained through heat treatment at different temperature (250 °C, 300 °C and 350 °C) for 2 h at a heating rate of 1 °C min^{-1} in air. The weight of samples was measured before preparation and after annealing and the mass loading of active materials was about 0.33 mg cm^{-2} if the corrosion effect of solution on Ni foams is neglected.

Characterizations

The structure and morphology of obtained samples were examined by field-emission scanning electron microscopy (FE-SEM, Zeiss Ultra Plus), transmission electron microscopy (TEM), high-resolution transmission electron microscopy (HR-TEM) (JEOL JEM-2100F with an acceleration voltage of 200 kV). Powder X-ray diffraction (XRD) (Cu K, = 1.5406 Å) was obtained on a Rigaku Ultima IV X-ray diffractometer. X-ray photoelectron spectroscopy (XPS) (AXIS ULTRA DLD, Kratos, Japan) was performed to analyze the surface chemical composition and valance states of the samples. Thermogravimetric analysis (TGA) (Pyris 1 TGA) was carried out with a temperature ramp of 10 °C min^{-1}. Raman spectrum (laser excitation λ_{exc} = 532 nm) was utilized to investigate the crystallographic texture. To determine the bulk composition of the whole samples, the ICP atomic emission spectrometer (ICP-AES) was employed in the experiment (shown in the ESI, Table S1†).

Electrochemical measurements

The electrochemical measurements of the NiO/$Ni_xCo_{3-x}O_4$ nanosheet/nanowire composite structure were carried out through a three-electrode cell in a 1 M KOH aqueous electrolyte, with the platinum plate electrode and Hg/HgO electrode as the counter and reference electrode. Cyclic voltammetry (CV), electrochemical impedance spectroscopy (EIS) tests and galvanostatic charge–discharge measurements were performed on CHI760B Electrochemical Workstation. The electrochemical capacitance was calculated as the following equation:[19]

$$C = \frac{I\Delta t}{A\Delta V}, \quad (1)$$

where C (mF cm^{-2}) is the electrochemical capacitance of the electrode, I (A) represents the current density, t (s) is the discharging time, ΔV (V) is the discharging potential range, and A (cm^2) is the area of the active material in the electrode.

Results and discussion

The typical XRD pattern of the NiO/$Ni_xCo_{3-x}O_4$ porous nanowire/porous ultrathin nanosheet composite structure annealed at 300 °C is shown in Fig. 1. For the NiO, the five peaks

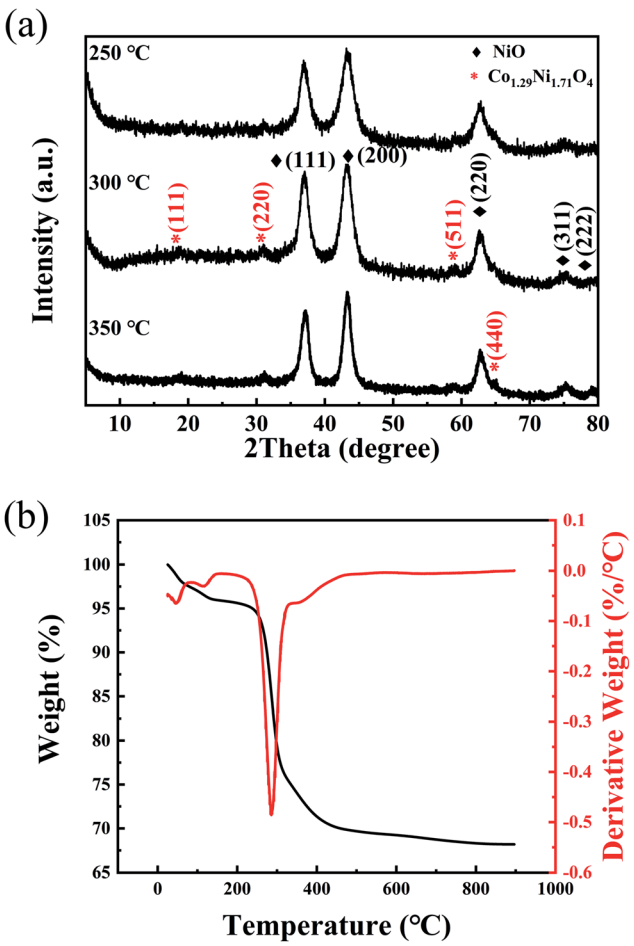

Fig. 1 (a) XRD patterns of the NiO/$Ni_xCo_{3-x}O_4$ nanosheet/nanowire composite structures. From the top to the bottom, the spectra corresponds to the samples annealed at 250 °C, 300 °C and 350 °C. (b) TGA (black) and DTG (red) curves of the precursor measured in air from room temperature to 900 °C at a heating rate of 10 °C min^{-1}.

at 37.3°, 43.4°, 63.0°, 75.6° and 79.6° due to the (111), (200), (220), (311) and (222) diffraction of nickel oxide layers can be clearly seen (JCPDS card no. 75-0197). The other peaks at 18.8°, 31.0°, 58.9°and 64.8° can be well indexed to as (111), (220), (511) and (440) characteristic diffraction of the $Co_{1.29}Ni_{1.71}O_4$ (JCPDS card no. 40-1191), implying that cobalt ions have been successfully doped into spinel oxide structure under the present conditions. The XRD patterns of samples annealed at 250 °C and 350 °C are similar to the pattern of the sample annealed at 300 °C, which indicates that the precursors start to transform to NiO and $Ni_xCo_{3-x}O_4$ at 250 °C.

In order to further substantiate the $NiO/Ni_xCo_{3-x}O_4$ formation, the TGA/DTG measurements were used to evaluate the functional relationship between the mass change and the temperature. Fig. 1b shows the TGA curves of the as-prepared precursor measured from room temperature to 900 °C. The initial weight losses accompanied by an endothermic reaction below 150 °C was assigned to the loss of adsorbed water and the evaporation of intercalated water molecules.[20] On further increasing the temperature, the major weight loss (20–22%) occurred in between 220–340 °C, which may be due to the decomposition reaction of nickel cobalt hydroxide precursor and the crystallization of $NiO/Ni_xCo_{3-x}O_4$.[21] To further substantiate the TGA results, DTG analyses is also given in Fig. 1b. The observed endothermic peaks below 150 °C is due to the removal of adsorbed water molecules in the structural water of nickel cobalt hydroxide precursor. Similarly, the formation of $NiO/Ni_xCo_{3-x}O_4$ porous nanowire/porous ultrathin nanosheet composite structure by the decomposition of hydroxide is confirmed through the obtained endothermic peak at 285 °C. In addition, a weight loss of about 6 wt% in the temperature range between 340 °C and 470 °C arises in the TGA curve with a step existing at about 350 °C in the DTG curve, which is attributed to the reaction between O_2 and hydrocarbons remained on surface of the sample.

The surface chemical composition and atomic valence states of the composite nanostructures can be further analyzed by XPS. Fig. 2a presents the full XPS spectrum of the $NiO/Ni_xCo_{3-x}O_4$ porous nanosheet/nanowire composite structure annealed at 300 °C. The XPS analysis of $NiO/Ni_xCo_{3-x}O_4$ porous structure shows that the atomic percentages on the sample surface of Ni, Co and O are 25.81%, 5.00% and 43.35%, indicating that Ni is enriched on the surface of the composite structure. The high resolution Ni 2p and Co 2p XPS peaks are shown in Fig. 2b and c. In Ni 2p spectra for the sample annealed at 250 °C, two sets of broad signals corresponding to Ni $2p_{3/2}$ (855.1 eV) and Ni $2p_{1/2}$ (872.6 eV) are observed, which demonstrates that the elemental Ni is in a range of typical Ni^{2+} or Ni^{3+} bound to oxygen.[22,23] The intense satellite peaks indicate that the majority of nickel elements in the crystal lattice are Ni^{2+} cations.[24,25] The sample annealed at 300 °C has the more proportion of the Ni^{2+} than other samples which annealed at 250 °C and 350 °C. In the Co 2p spectra, two sets of broad signals consistent with Co $2p_{3/2}$ (779.7 eV) and Co $2p_{1/2}$ (794.9

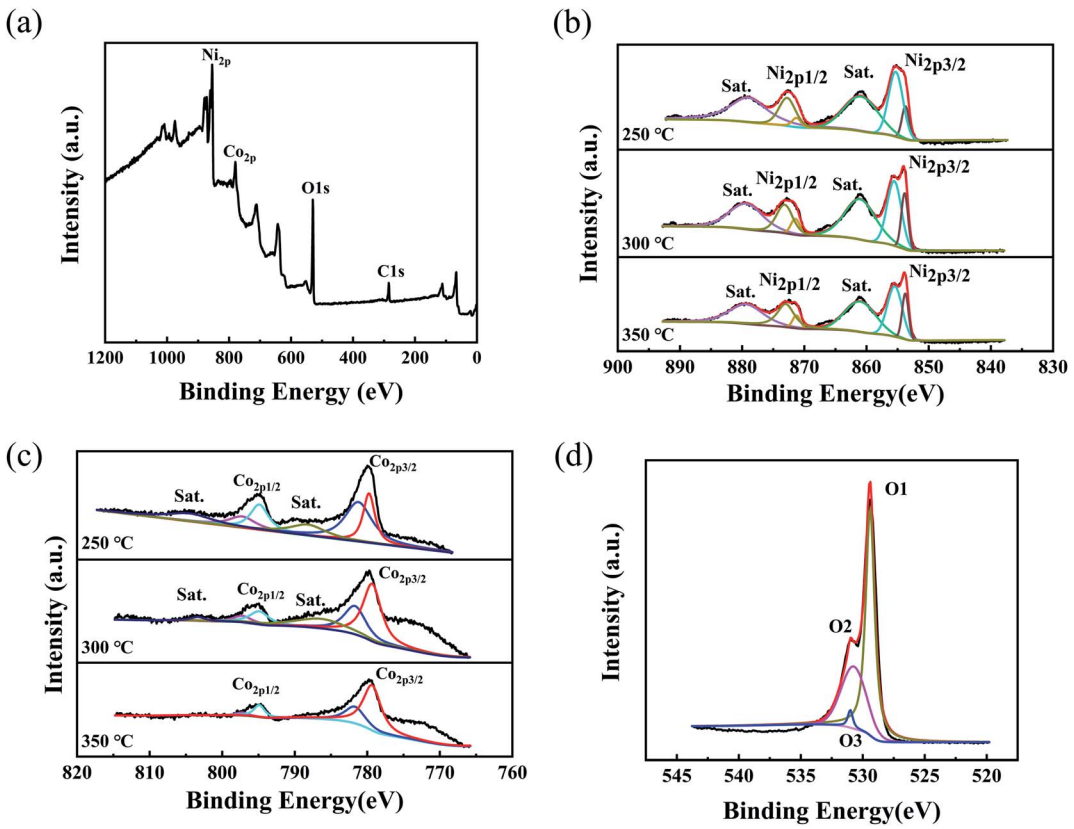

Fig. 2 (a) XPS survey spectrum, (b) the high-resolution XPS spectrum of Ni 2p, (c) the high-resolution XPS spectrum of Co 2p, and (d) XPS spectrum of O 1s for the $NiO/Ni_xCo_{3-x}O_4$ nanostructures.

eV) are observed. The spectra are also composed of two spin–orbit doublets Co^{3+} and Co^{2+}. The proportions of Co^{3+} in the sample annealed at 300 °C and 350 °C increased from 41.0% (the sample annealed at 250 °C) to 64.1% and 69.6%, suggesting there were more and more Co^{3+} ions in the sample after higher anneal temperature. The result suggests that a larger number of cobalt cations were oxidized from the Co^{2+} to the Co^{3+} spectra and the decay of satellite peaks also demonstrates this results.[25–27] To determine the bulk composition of the whole samples, the ICP atomic emission spectrometer (ICP-AES) was employed in the experiment (shown in the ESI, Table S1†). The mass percentages of Co in the whole samples increased from 0.202% annealed at 250 °C to 0.268% at 300 °C and 0.387% at 350 °C, which indicated that nickel cobalt hydroxide precursor more fully decomposed and $NiO/Ni_xCo_{3-x}O_4$ crystalized more completely with the increasing annealing temperature.

By using a Gaussian fitting method, the high-resolution spectrum for the O 1s region (Fig. 2d) shows three oxygen contributions, which have been denoted as O1, O2, and O3. The O1 component located at 529.4 eV is typical of metal–oxygen bonds.[28] The O2 component at 531 eV is usually associated with oxygen in OH groups and the presence of this contribution in the O 1s spectrum indicates that the surface of the $NiCo_2O_4$ materials is hydroxylated to some extent as a result of either surface oxyhydroxide or the substitution of oxygen atoms at the surface by hydroxyl groups.[28,29] The O3 contribution corresponds to a higher number of defect sites with low oxygen coordination in the material with small particle sizes.[30] These results show that the surface of the 3D $NiO/Ni_xCo_{3-x}O_4$ nanosheets and 1D $NiO/Ni_xCo_{3-x}O_4$ nanowires has a composition containing Co^{2+}, Co^{3+}, Ni^{2+} and Ni^{3+}, which is in good agreement with the results in the literature for other nickel cobalt oxide.[31,32] Besides, the atomic proportions of C remained on the samples surface decreased from 28.20% annealed at 250 °C to 25.84% at 300 °C and 22.41% at 350 °C, which corresponds to the results of DTG analyses.

Raman spectrum was utilized to investigate the graphitization degree of carbon remained on the simple surface. The Raman spectra (Fig. S1a†) of the sample annealed at 300 °C displayed two characteristic peaks at 1332 and 1590 cm^{-1} which are assigned to the typical D (disordered carbon) and G (sp^2-hybridized C atoms of the graphitic carbon) bands, respectively.[33–35] The I_D/I_G ratios (the intensity ratio of two bands) is reported to investigate the structural order degree of carbons, and the I_D/I_G value of 1.0 is generally typical of amorphous carbons.[33,34] The calculated I_D/I_G value is 0.28, which proves the good graphitization degree of carbon remained in the composite. The related papers have been cited. Furthermore, from the Raman spectra (Fig. S1b†) of the sample annealed at 250 °C and 350 °C, peaks at 187, 534 and 647 cm^{-1} correspond to the characteristic peaks for F_{2g}, F_{2g} and A_{1g} stretching modes of spinel $Ni_xCo_{3-x}O_4$ on the nickel foam.[36]

The morphologies of the $NiO/Ni_xCo_{3-x}O_4$ nanosheet/nanowire are shown in Fig. 3 at different magnification. It is apparent that the porous ultrathin nanosheets mainly vertically or aslant attached on the nickel foam are free-standing and mutual staggered, forming a highly open nanostructure with nanowires above them. This composite nanostructure can enlarge the contact surface area with electrolyte and facilitate the penetration of the ions, promoting the velocity of redox reaction.[37] The high-magnification TEM images shown as Fig. 3c and d reveal that the diameter of nanowires is about 50–80 nm and the mesopores are also present both in the ultrathin nanosheets and nanowires with a size of 5 to 8 nm. This kind of ultrathin porous structure in the nanohybrids is very important, as it facilitates the fast mass transport of electrolytes within the electrodes for quick redox reaction.[31,38] Fig. 3e and f show a high-resolution TEM (HRTEM) image. The considerably distinct lattice spacing of 0.29 nm in nanosheets and nanowires is in good accordance with the (220) plane of $Co_{1.29}Ni_{1.71}O_4$. The lattice spacing of 0.24 nm is due to the (222) plane of $Co_{1.29}Ni_{1.71}O_4$ plane whose diffraction peak was covered up in XRD pattern. The measured angle between the (220) plane and the (222) plane from FFT pattern (Fig.S3†) is fit well with the theoretical value. They further indicate that $Ni_xCo_{3-x}O_4$ has been successfully prepared under the present conditions.

Further, we evaluated the electrochemical performance of the as-prepared $NiO/Ni_xCo_{3-x}O_4$ nanohybrids in a three-electrode test cell. The capacitive behavior of the electrode material is generally characterized using cyclic voltammetry (CV) curves. Fig. 4a presents typical CV curves of the $NiO/Ni_xCo_{3-x}O_4$ nanohybrids samples anneal at 300 °C in a 1 M KOH electrolyte at various scan rates between 0.0 and 0.5 V. Two redox peaks can be observed in the curve at 5 mV s^{-1} scan rate. For electric double-layer capacitors, CV curves appear nearly rectangular. Our results thus indicate that the capacitance characteristics are mainly due to faradaic redox reactions.[39] For the $NiO/Ni_xCo_{3-x}O_4$ electrode materials, the surface faradaic reactions will proceed as:[40]

$$NiO + OH^- \leftrightarrow NiOOH + H_2O + e^- \quad (2)$$

$$Ni_xCo_{3-x}O_4 + OH^- + H_2O \leftrightarrow xNiOOH + 3-xCoOOH + e^- \quad (3)$$

$$CoOOH + OH^- \leftrightarrow CoO_2 + H_2O + e^- \quad (4)$$

To further evaluate the electrochemical properties and estimate the stable potential windows of the as-prepared $NiO/Ni_xCo_{3-x}O_4$ nanohybrids, galvanostatic charging and discharging tests of the films in 1 M KOH solution were performed using a Pt counter electrode and a mercury/mercuric oxide electrode. The charge–discharge curves (Fig. 4b) at different current densities from 1 to 5 mA cm^{-2} with potential window between 0.0 and 0.5 V display slight nonlinearities that are very distinct from those of typical pure double-layer capacitors. This result indicates the occurrence of faradaic reactions in the $NiO/Ni_xCo_{3-x}O_4$ composites.[41]

Good cycling stability is another important characteristic for high-performance supercapacitors. Fig. 4c reveals the cycle performance of the $NiO/Ni_xCo_{3-x}O_4$ nanohybrids samples measured at a current density of 5 mA cm^{-2} for 20 000 cycles. Among all electrodes prepared, the sample annealed in air at 300 °C displays the best electrochemical behavior, achieving

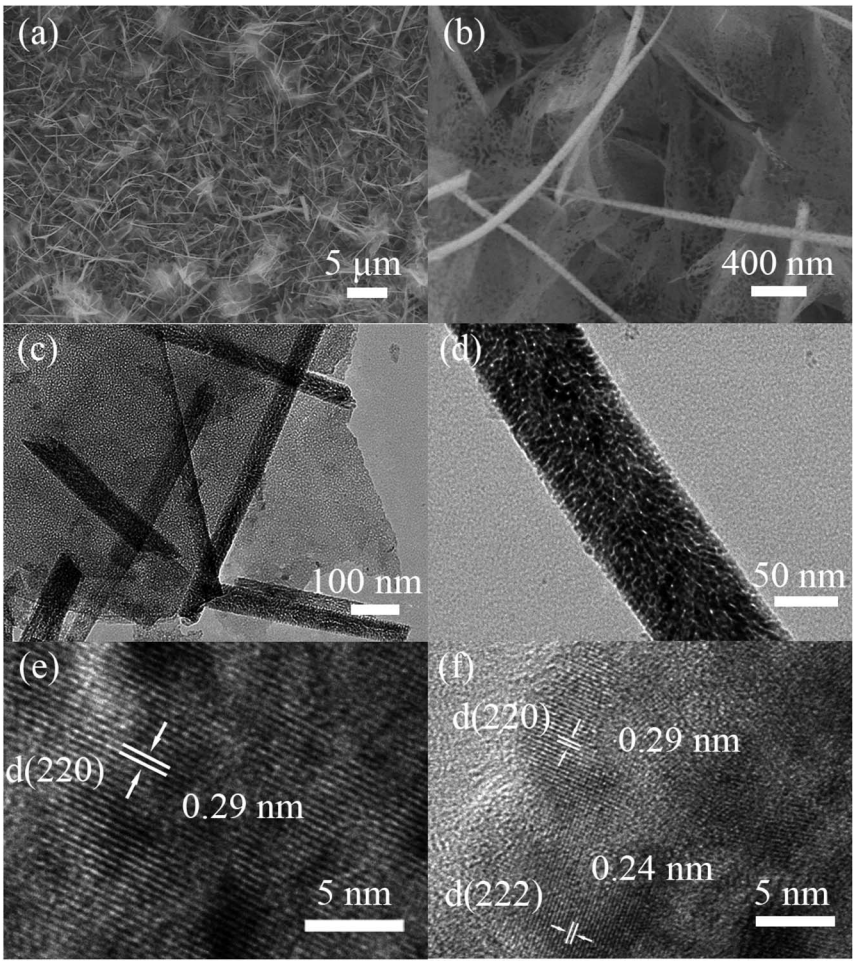

Fig. 3 Morphologies of the NiO/$Ni_xCo_{3-x}O_4$ composite nanostructures, (a) and (b) SEM images of the NiO/$Ni_xCo_{3-x}O_4$ composite materials; (c) and (d) TEM images of the NiO/$Ni_xCo_{3-x}O_4$ porous nanostructures; (e) HRTEM image of the NiO/$Ni_xCo_{3-x}O_4$ porous nanosheets; (f) HRTEM image of the NiO/$Ni_xCo_{3-x}O_4$ porous nanowires.

a specific capacitance of 270 mF cm^{-2} (about 810 F g^{-1}) at 5 mA cm^{-2}. Afterward, the capacitance retention was 88.89% of the max capacitance, indicating excellent long-term stability of the NiO/$Ni_xCo_{3-x}O_4$ composite electrode, which exceeds those of the previously reported Ni-based materials.[9,42] By comparison, the samples annealed at 250 °C and 300 °C presented much higher capacitance than sample annealed at 350 °C. These results highly highlight the vital roles of the cobalt ions and the presence of hydrocarbons into electrochemical active electrode materials.

Fig. 4d shows the rate performance of the sample annealed at 300 °C. The specific capacitances obtained were 220, 216, 180, 160 and 120 mF cm^{-2} at current densities of 1, 2, 5, 10 and 20 mA cm^{-2} respectively, which shows up better rate performance than single NiO materials.[43,44] Clearly, the specific surface capacitance gradually decreases with increasing current density. The specific capacitance decreases gradually with increasing current density, which can be attributed to the diffusion effect limiting the diffusion and migration of the electrolyte ions within the electrode at high electric current density because of the time constraint and only the outer active surface can be utilized for charge storage, resulting in low electrochemical utilization of the electroactive materials.[45–47]

To further study the different electrochemical performance after annealing and the decay of the specific capacitance after cycling tests, EIS measurements were carried out at an open circuit potential in a frequency ranging from 0.1 Hz to 100 kHz. As shown in Fig. 5, in the high-frequency region the intersections on the Z' axis represent the equivalent series resistance of capacitors (R_s) including the internal resistance of electrode materials, the ohmic resistance of the electrolyte and contact resistance between electrodes and current collectors.[10,48] Obviously, NiO/$Ni_xCo_{3-x}O_4$ nanohybrids at 300 °C annealing temperature has the smaller equivalent series resistance value than other NiO/$Ni_xCo_{3-x}O_4$ nanohybrids as shown in Fig. 5a, reflecting the optimum electronic and ionic conductivities of NiO with the presence of Ni_x-$Co_{3-x}O_4$ at 300 °C annealing temperature. This result is consistent with good cycle performance results of NiO/$Ni_xCo_{3-x}O_4$ composites. As shown in Fig. 5b, the electrode has a higher R_s and worse electric conductivity after cycling tests, leading to decay of the electrochemical performance. The inset SEM image with cracks further indicates volumetric changes after cycles.

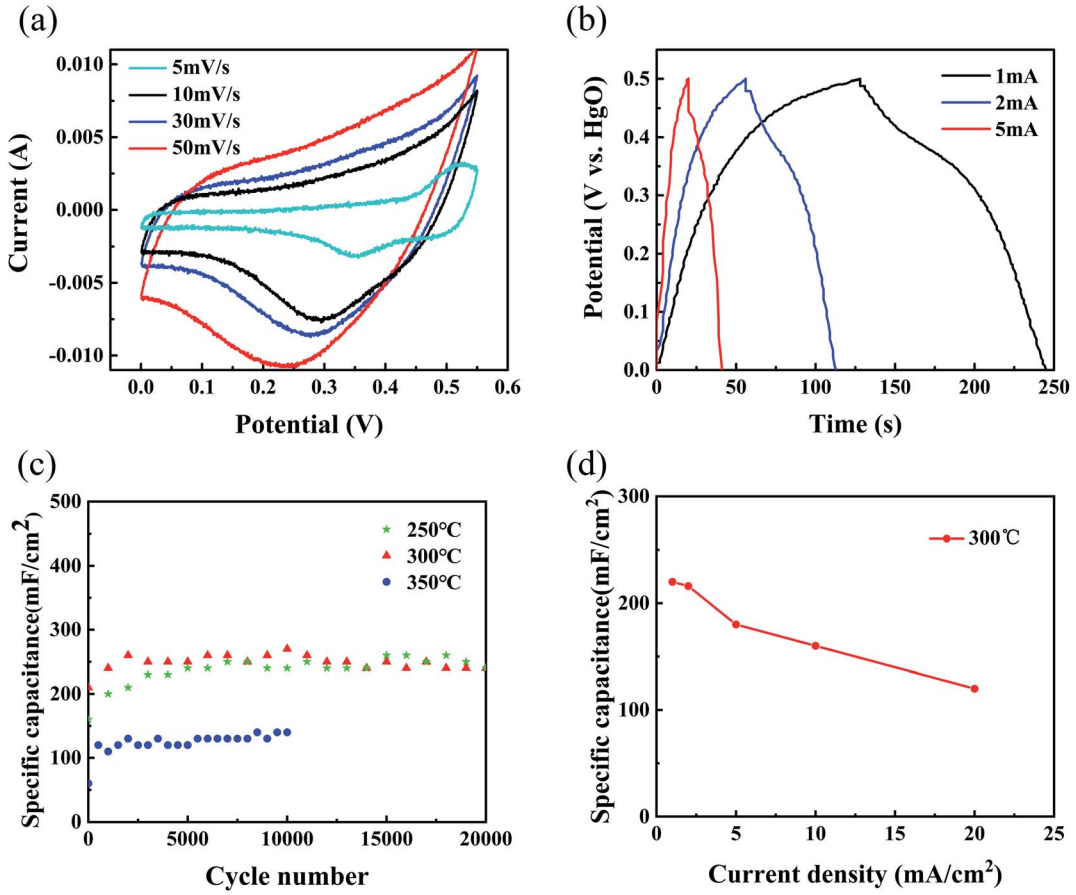

Fig. 4 Electrochemical characterization of the NiO/$Ni_xCo_{3-x}O_4$ composite electrode: (a) CV curves at different scan rates in 1 M KOH electrolyte (b) charge–discharge curves at different current densities (c) specific capacitance *versus* cycle number at constant current density of 5 mA cm^{-2} (d) the specific surface capacitance at various current densities after cycling.

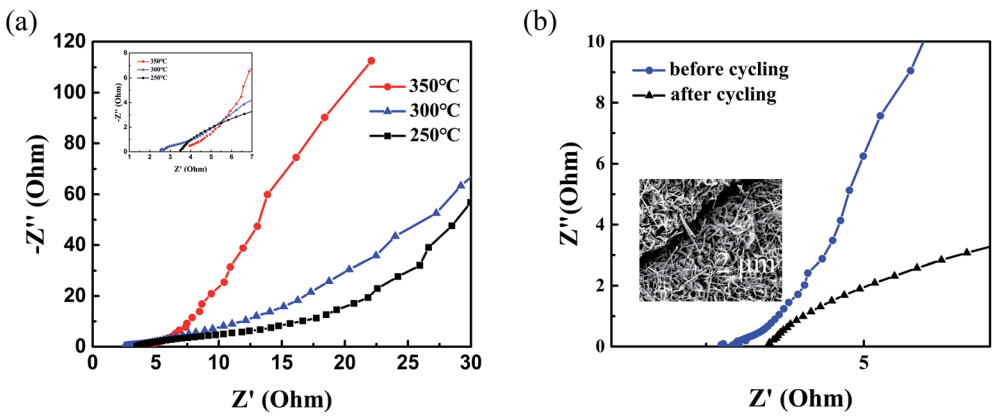

Fig. 5 (a) Nyquist plots of the NiO/$Ni_xCo_{3-x}O_4$ composite electrode at different annealing temperature. The inset is the coordinate reduced image. (b) Nyquist plots before and after cycling tests of the NiO/$Ni_xCo_{3-x}O_4$ composite electrode at current density of 5 mA cm^{-2} for 20 000 cycles. The inset is the SEM image after cycling tests.

Conclusion

In summary, a facile and low cost synthesis approach was adopted to synthesize cobalt doped nickel oxide porous ultrathin nanosheet/porous nanowire composite structure. Moreover, the as-prepared sample displays excellent electrochemical performance, the maximum specific capacitance of 270 mF cm^{-2} and capacitance retention of 88.9% after 20 000 cycles. Such a simple and cost-effective synthetic approach would open new doors for the development of a serial of high-quality NiCo-based materials, and offer promising applications for high-performance energy-storage devices.

Conflicts of interest

There are no conflicts of interest to declare.

Acknowledgements

We acknowledge the support of the Natural Science Foundation of China (grant no. 11574203 and 11174197).

References

1 H.-J. Choi, S.-M. Jung, J.-M. Seo, D. W. Chang, L. Dai and J.-B. Baek, *Nano Energy*, 2012, **1**, 534–551.
2 P. Huang, C. Lethien, S. Pinaud, K. Brousse, R. Laloo, V. Turq, M. Respaud, A. Demortière, B. Daffos, P. L. Taberna, B. Chaudret, Y. Gogotsi and P. Simon, *Science*, 2016, **351**, 691–695.
3 J. R. Miller and P. Simon, *Science*, 2008, **321**, 651–652.
4 P. Simon and Y. GoGotSi, *Nat. Mater.*, 2008, **7**, 845–854.
5 A. Aricò, P. Bruce, B. Scrosati, J. Tarascon and W. V. Schalkwijk, *Nat. Mater.*, 2005, **4**, 366–377.
6 J. Yang, C. Yu, X. Fan and J. Qiu, *Adv. Energy Mater.*, 2014, **4**, 100761.
7 C. Chen, C. Chen, P. Huang, F. Duan, S. Zhao, P. Li, J. Fan, W. Song and Y. Qin, *Nanotechnology*, 2014, **25**, 504001.
8 W. Yu, B. Q. Li and S. J. Ding, *Nanotechnology*, 2016, **27**, 075605.
9 B. Dong, H. Zhou, J. Liang, L. Zhang, G. Gao and S. Ding, *Nanotechnology*, 2014, **25**, 435403.
10 R. Li, Z. Hu, X. Shao, P. Cheng, S. Li, W. Yu, W. Lin and D. Yuan, *Sci. Rep.*, 2016, **6**, 18737.
11 S. Nandy, U. N. Maiti, C. K. Ghosh and K. K. Chattopadhyay, *J. Phys.: Condens. Matter*, 2009, **21**, 115804.
12 S. Liu, S. C. Lee, U. Patil, I. Shackery, S. Kang, K. Zhang, J. H. Park, K. Y. Chung and S. Chan Jun, *J. Mater. Chem. A*, 2017, **5**, 1043–1049.
13 L. Xie, Z. Hu, C. Lv, G. Sun, J. Wang, Y. Li, H. He, J. Wang and K. Li, *Electrochim. Acta*, 2012, **78**, 205–211.
14 Z. Chang, H. Li, H. Tang, X. Z. Yuan and H. Wang, *Int. J. Hydrogen Energy*, 2009, **34**, 2435–2439.
15 G. Zhang and X. W. David Lou, *Sci. Rep.*, 2013, **3**, 1470.
16 H. Chen, L. Hu, M. Chen, Y. Yan and L. Wu, *Adv. Funct. Mater.*, 2014, **24**, 934–942.
17 R. R. Salunkhe, K. Jang, S.-w. Lee and H. Ahn, *RSC Adv.*, 2012, **2**, 3190–3193.
18 Y. Zhao, L. Hu, S. Zhao and L. Wu, *Adv. Funct. Mater.*, 2016, **26**, 4085–4093.
19 M. Jin, G. Zhang, F. Yu, W. Li, W. Lu and H. Huang, *Phys. Chem. Chem. Phys.*, 2013, **15**, 1601–1605.
20 L. Qian, L. Gu, L. Yang, H. Yuan and D. Xiao, *Nanoscale*, 2013, **5**, 7388–7396.
21 B. Cui, H. Lin, J.-B. Li, X. Li, J. Yang and J. Tao, *Adv. Funct. Mater.*, 2008, **18**, 1440–1447.
22 A. N. Mansour, C. A. Melendres, M. Pankuch and R. A. Brizzolara, *J. Electrochem. Soc.*, 1994, **141**, L69–L71.
23 X. Yu, Z. Sun, Z. Yan, B. Xiang, X. Liu and P. Du, *J. Mater. Chem. A*, 2014, **2**, 20823–20831.
24 A. Shanmugavani and R. K. Selvan, *Electrochim. Acta*, 2016, **189**, 283–294.
25 J.-G. Kim, D. L. Pugmire, D. Battaglia and M. A. Langell, *Appl. Surf. Sci.*, 2000, **165**, 70–84.
26 S. Cobo, J. Heidkamp, P. A. Jacques, J. Fize, V. Fourmond, L. Guetaz, B. Jousselme, V. Ivanova, H. Dau, S. Palacin, M. Fontecave and V. Artero, *Nat. Mater.*, 2012, **11**, 802–807.
27 Y. Q. Liang, Z. D. Cui, S. L. Zhu, Z. Y. Li, X. J. Yang, Y. J. Chen and J. M. Ma, *Nanoscale*, 2013, **5**, 10916–10926.
28 T. Choudhury, S. O. Saied, J. L. Sullivan and A. M. Abbot, *J. Phys. D: Appl. Phys.*, 1989, **22**, 1185–1195.
29 Y. E. Roginskaya, O. V. Morozova, E. N. Lubnin, Y. E. Ulitina, G. V. Lopukhova and S. Trasatti, *Langmuir*, 1997, **13**, 4621–4627.
30 V. M. Jimenez, A. Fernandez, J. P. Espinos and A. R. Gonzalez-Elipe, *J. Electron Spectrosc. Relat. Phenom.*, 1995, **71**, 61–71.
31 C. Yuan, J. Li, L. Hou, X. Zhang, L. Shen and X. W. D. Lou, *Adv. Funct. Mater.*, 2012, **22**, 4592–4597.
32 J. F. Marco, J. R. Gancedo, M. Gracia, J. L. Gautier, E. I. Ríos, H. M. Palmer, C. Greaves and F. J. Berry, *J. Mater. Chem.*, 2001, **11**, 3087–3093.
33 L. Miao, D. Zhu, M. Liu, H. Duan, Z. Wang, Y. Lv, W. Xiong, Q. Zhu, L. Li, X. Chai and L. Gan, *Chem. Eng. J.*, 2018, **347**, 233–242.
34 L. Miao, D. Zhu, M. Liu, H. Duan, Z. Wang, Y. Lv, W. Xiong, Q. Zhu, L. Li, X. Chai and L. Gan, *Electrochim. Acta*, 2018, **274**, 378–388.
35 D. Zhu, J. Jiang, D. Sun, X. Qian, Y. Wang, L. Li, Z. Wang, X. Chai, L. Gan and M. Liu, *J. Mater. Chem. A*, 2018, **6**, 12334–12343.
36 H. Wang, J. Guo, C. Qing, D. Sun, B. Wang and Y. Tang, *Chem. Commun.*, 2014, **50**, 8697–8700.
37 Y. You, M. Zheng, L. Ma, X. Yuan, B. Zhang, Q. Li, F. Wang, J. Song, D. Jiang, P. Liu, L. Ma and W. Shen, *Nanotechnology*, 2017, **28**, 105604.
38 J. Yan, W. Sun, T. Wei, Q. Zhang, Z. Fan and F. Wei, *J. Mater. Chem.*, 2012, **22**, 11494–11502.
39 L. Ma, M. Zheng, S. Liu, Q. Li, Y. You, F. Wang, L. Ma and W. Shen, *Chem. Commun.*, 2016, **52**, 13373–13376.
40 F.-X. Ma, L. Yu, C.-Y. Xu and X. W. Lou, *Energy Environ. Sci.*, 2016, **9**, 862–866.
41 S. Zhang and N. Pan, *Adv. Energy Mater.*, 2015, **5**, 1401401.
42 J. Ji, L. L. Zhang, H. Ji, Y. Li, X. Zhao, X. Bai, X. Fan, F. Zhang and R. S. Ruoff, *ACS Nano*, 2013, **7**, 6237–6243.
43 C. Yuan, X. Zhang, L. Su, B. Gao and L. Shen, *J. Mater. Chem.*, 2009, **19**, 5772–5777.
44 S. I. Kim, J. S. Lee, H. J. Ahn, H. K. Song and J. H. Jang, *ACS Appl. Mater. Interfaces*, 2013, **5**, 1596–1603.
45 J. Yan, Z. Fan, W. Sun, G. Ning, T. Wei, Q. Zhang, R. Zhang, L. Zhi and F. Wei, *Adv. Funct. Mater.*, 2012, **22**, 2632–2641.
46 H. Jiang, T. Zhao, C. Li and J. Ma, *J. Mater. Chem.*, 2011, **21**, 3818–3823.
47 Z. J. Lao, K. Konstantinov, Y. Tournaire, S. H. Ng, G. X. Wang and H. K. Liu, *J. Power Sources*, 2006, **162**, 1451–1454.
48 Z. Chen, Z. Wan, T. Yang, M. Zhao, X. Lv, H. Wang, X. Ren and X. Mei, *Sci. Rep.*, 2016, **6**, 25151.